Magnetoluminescence

R. Blandford, Y. Yuan, M. Hoshino,
L. Sironi

Abstract Pulsar Wind Nebulae, Blazars, Gamma Ray Bursts and Magnetars all contain regions where the electromagnetic energy density greatly exceeds the plasma energy density. These sources exhibit dramatic flaring activity where the electromagnetic energy distributed over large volumes, appears to be converted efficiently into high energy particles and γ-rays. We call this general process magnetoluminescence. Global requirements on the underlying, extreme particle acceleration processes are described and the likely importance of relativistic beaming in enhancing the observed radiation from a flare is emphasized. Recent research on fluid descriptions of unstable electromagnetic configurations are summarized and progress on the associated kinetic simulations that are needed to account for the acceleration and radiation is discussed. Future observational, simulation and experimental opportunities are briefly summarized.

1 Introduction and Context

The discovery of cosmic rays over a century ago (Hess 1912), of double radio sources and radio supernova remnants in the 1940s (Reber and Greenstein 1947), of X-ray Binaries (Giacconi et al 1962), quasars (Schmidt 1963), pulsars (Hewish et al 1968) and Gamma Ray Bursts (Klebesadel et al 1973) in the 1960s, magnetars in the 1970s and Fast Radio Bursts (Lorimer et al 2007) a decade ago have revealed

R. Blandford
KIPAC, Stanford University, Stanford, CA 94305, USA E-mail: rdb3@stanford.edu

Y. Yuan
Lyman Spitzer, Jr. Postdoctoral Fellow, Dept. Astrophysical Sciences, Princeton University, Princeton, NJ 08540, USA E-mail: yajiey@astro.princeton.edu

M. Hoshino
University of Tokyo, 7-3-1 Hongo, Bunkyo, Tokyo 113-0033
E-mail: hoshino@eps.s.u-tokyo.ac.jp

L. Sironi
Department of Astronomy, Columbia University, New York, NY, 10027
E-mail: lsironi@astro.columbia.edu

the nonthermal universe. This is a very different world from the thermal universe studied by stellar astronomers. Roughly ten percent of the total gravitational energy that is released in the universe— principally by black holes and neutron stars — (and nearly one percent of the nuclear energy) is carried off or radiated by relativistic particles and these have to be accelerated. The only way to accelerate charges is through the application of electric field. However, it is hard to sustain large enough electrostatic field for this purpose and moving or rapidly changing magnetic field is generally invoked to generate the necessary potential differences.

While the prodigious power of high energy processes has long been appreciated (e.g., Burbidge 1956), it is their rapid variability that has drawn more attention in recent years. This takes us into the regime of *extreme astrophysics*. The associated particle acceleration has to be extremely potent and the steady, stochastic energy conversion of traditional Fermi acceleration is not an option. New mechanisms that can operate in a great variety of sites are needed. A common characteristic of many of these cosmic sources is the extraction of rotational and gravitational energy from a *prime mover* by large scale electromagnetic field. In the case of a pulsar or a black hole it is rotational energy. in the case of a magnetar it is ultimately gravitational energy. In the case of an accretion disk, it is both. We are not confident that this is always the case, but it is beginning to look that way.

Inevitably, this electromagnetic field is accompanied by plasma, at the very least sufficient to supply the space charge and current, and this plasma is ultimately expected to share the electromagnetic energy. Two quite different pathways for this energy conversion are available. The first is *dissipation*. Electromagnetic energy is converted ("prodigally") to particle energy at a rate $\mathbf{E} \cdot \mathbf{j}$ per unit volume, and entropy is created. The second is *plasma acceleration*. The electromagnetic force density $\rho \mathbf{E} + \mathbf{j} \times \mathbf{B}$ increases the bulk kinetic energy of all of the plasma ("industriously"). This may be very efficient but does not directly produce dramatic particle acceleration and rapid variability. This may happen later, for example when the bulk flow passes through a strong shock front. (Rapidly variation from the solar wind stimulated Gold (1955) to make the radical proposal that collisionless plasma could form essentially discontinuous shock fronts.) Of course, electromagnetic field must be present at the shock (in order to mediate the shock in the absence of collisions), but this is probably independent of the electromagnetic field associated with the prime mover.

Observations of rapidly variable sources, especially by γ-ray telescopes, strongly suggest the presence of regions of relatively high electromagnetic energy density which is efficiently dissipated and where electrons and positrons are efficiently accelerated up to their radiation reaction limits on a light crossing timescale. The available electromagnetic energy is seized, "plutocratically", by a small minority of particles and not, "democratically", by the bulk of the plasma. Additional features, such as bulk relativistic motion, may be present and needed to account for the observations. We call this general phenomenon *magnetoluminescence* (Blandford et al 2014, 2015) by analogy with the flashes of light seen from collapsing bubbles created by ultrasound — sonoluminescence (Brenner et al 2002). (This phenomenon can also be produced naturally by pistol shrimp (Lohse et al 2001).) Similar mechanisms may have to be invoked to account for the acceleration of cosmic rays with PeV (10^{15} eV), EeV (10^{18} eV) and even ZeV (10^{21} eV) energy.

Our goal in this chapter is to complement some of the other chapters in this volume by providing a general description of extreme particle acceleration that

brings out the common features present in the many sources where magnetoluminescence is seen. In the rest of the chapter, we first give a quick summary of the challenges brought up by various extreme particle accelerators in §2, then discuss some basic principles of particle acceleration in §3 and global considerations of electromagnetic dissipation in §4. We show relativistic MHD and kinetic modeling of the possible processes underlying magnetoluminescence in §5 and §6, respectively. We conclude with a discussion of future observational, simulation and experimental prospects in §7.

2 Extreme Particle Accelerators

2.1 Pulsars and their Nebulae

A striking and relatively recent example of extreme particle acceleration is provided by the γ-ray flares in the Crab Nebula, best observed by Fermi (e.g., Buehler and Blandford 2014). The nebula itself, which has to be our best laboratory for high energy astrophysics, has been observed over the entire electromagnetic spectrum from $\lesssim 100\,\mathrm{MHz}$ to $\gtrsim 1.5\,\mathrm{TeV}$ (see, e.g., Hester 2008, for a review). It has been powered for the past 963 y. by the central pulsar with its $\sim 30\,\mathrm{Hz}$ rotation frequency. The pulsar loses energy at a rate $\sim 5 \times 10^{31}\,\mathrm{W}$, roughly four times the current bolometric power ($\sim 1.3 \times 10^{31}\,\mathrm{W}$) of the nebula, which peaks around $\sim 10\,\mathrm{eV}$. The power assuredly takes the form of an electromagnetic Poynting flux leaving the surface of the neutron star, becoming a relativistic electromagnetic wind with properties that are best defined by the ratio of the electromagnetic energy flux to the particle energy flux (usually assumed to comprise pairs, though ion-dominated winds are possible), σ, the outflow Lorentz factor and a description of the variation of the outflow with latitude. The Crab Nebula demonstrates that electromagnetic conversion of prime-mover power into relativistic electrons and positrons can be very efficient. However, it has not told us where this conversion takes place and there are viable models that locate this conversion all the way from the pulsar light cylinder to the outer nebula (e.g., Kirk et al 2009; Arons 2012).

The Crab pulsar wind must decelerate from the speed of light to the expansion speed of the supernova remnant $\sim 1500\,\mathrm{km\,s^{-1}}$. This is commonly supposed to begin at a strong, relativistic, collisionless shock front located where the outflow momentum flux matches the ambient nebula pressure at a radius $\sim 3 \times 10^{15}\,\mathrm{m} \sim 0.1\,\mathrm{pc}$ (Rees and Gunn 1974; Kennel and Coroniti 1984). If, as expected, the strength of the wind decreases significantly with latitude, the shock surface will be quite oblate (e.g., Komissarov and Lyubarsky 2003). This is compatible with the observation of an equatorial torus at X-ray energies (Weisskopf et al 2000).

However, there is no observation that suggests the presence of a shock outside the equatorial zone. The "inner knot", a compact feature located $0.65''$ southeast of the Crab pulsar in infrared and optical images (Hester et al 1995; Rudy et al 2015), has been modeled as a point on the oblique part of the termination shock in the polar region(Komissarov and Lyubarsky 2004; Komissarov and Lyutikov 2011), but there is some evidence that it may be associated with the low latitude section of the pulsar wind where the effective magnetization becomes low because of the alternating magnetic flux in a "striped" wind (Lyutikov et al 2016a; Yuan

and Blandford 2015). At higher latitudes, it is consistent with $\sigma \gg 1$ at this radius (as we must assume for the mechanisms we are reviewing here) so that the shock is weak — there may be several of them — and most of the deceleration happens gradually. Given this model, the magnetic field strength is $\sim 100\,\mathrm{nT}$ here, decreasing to $\sim 30\,\mathrm{nT}$ in the body of the nebula.

The observed γ-ray flares (e.g., Buehler and Blandford 2014) happen with a cadence $\sim 1\,\mathrm{y}$ and have only been seen at energies $\sim 300\,\mathrm{MeV}$ and there are no associated pulsar timing glitches. Variation, on timescales as short as a few h has been reported. The peak isotropic luminosity is roughly $10^{29}\,\mathrm{W}$ and the energy radiated is $\sim 10^{34}\,\mathrm{J}$. The flares and secular observations (Wilson-Hodge et al 2011) demonstrate that the energy conversion is intermittent not steady and that the mechanism can be locally cataclysmic.

2.2 Blazars

Most galaxies, at least as massive as our Galaxy, possess nuclei surrounding a massive ($\sim 10^6 - 10^{10}\,\mathrm{M_\odot}$) black hole which become *active* either when they are supplied with gas that is efficiently accreted or the holes are spun up and the rotational energy is tapped (e.g., Meier 2012). A common expression of this activity is the formation of a pair of antiparallel *relativistic jets*, with Lorentz factors $\Gamma \sim 10$, presumably directed along the hole's rotation axis, at least initially. The presence of these jets was originally inferred from the observations of large double radio sources straddling the optical image of the host galaxy, which they supply with energy, momentum and mass. However, jets are now observed throughout the electromagnetic spectrum, most notably at γ-ray energies (see, e.g., Madejski and Sikora 2016, for a review). As the outflows are relativistic close enough to the hole, jet emission is strongly beamed and a small minority of sources are observed to be unusually bright as they are directed towards us. These are called *blazars* and they can dominate a flux-limited sample. Observations made using Very Long Baseline Interferometry (VLBI) at cm and mm wavelengths have confirmed that these jets are already collimated on scales $\lesssim 100 - 1000$ black hole gravitational radii (Marscher et al 2008) and we are now on the threshold of resolving the curved spacetime around the black hole (Broderick et al 2015; Fish et al 2016). Relativistic jets are now acknowledged as being powered by the inner accretion disk and the black hole spin energy but the relative importance of these two sources is debated.

Blazars are frequently divided into two types, *BL Lac objects*, or BLL, and *Flat Spectrum Radio Quasars* or FSRQ. BLL are low total power objects and mostly local; FSRQ are high power quasars which can outshine the host galaxy and are mostly at cosmological redshifts. Both classes exhibit remarkable GeV/TeV flares with source variation times as short as $\sim 2 - 3$ minutes (e.g., Albert et al 2007; Aharonian et al 2007; Aleksić et al 2011; Ackermann et al 2016). This suggests that the emission originates very close to the jet source. However, there is a lower bound on the radius where the particle acceleration and emission can occur due to absorption involving pair production on soft photons. This radius can be calculated assuming QED (in which we should have absolute confidence!) and this defines the *gammasphere* (Blandford and Levinson 1995). As with the Crab Nebula, there are viable models with emission radii ranging from the gammasphere to the sites of recollimation located $\gtrsim 100\,\mathrm{pc}$ from the hole. There is now good evidence that the

γ-rays are produced before and within the radio emission (Max-Moerbeck et al 2014).

2.3 Gamma Ray Bursts

Most *Gamma Ray Bursts*, GRB, are cosmologically distant and release the energy equivalent of a significant fraction of a stellar mass (see, e.g., Kouveliotou et al 2012, for a review). There are also two types: the *short bursts* lasting $\lesssim 2\,$s are conjectured to be neutron star binaries, merging under gravitational radiation reaction and potentially observable by LIGO/VIRGO; the *long bursts* are convincingly associated with a subset of core-collapse supernovae tentatively identified with progenitors that have lost their helium and hydrogen envelopes although other factors could easily be relevant. GRBs are also relativistic jets (with $\Gamma \sim 100 - 1000$). They are collimated by the collapsing star in the long bursts; the jets from short bursts may be collimated by a very dense accretion disk.

The prompt γ-ray emission from GRBs is often found to be variable on timescales as short as $\sim 10\,$ms. The *afterglow*, observed throughout the electromagnetic spectrum, is formed later when the jets are decelerated by interaction with the circumstellar medium.

One common feature of models of long and short bursts and AGN (and, also, Galactic superluminal sources (Mirabel and Rodríguez 1999)) is the realization that the accreting gas near the hole cannot cool requiring the formation of a thick orbiting torus at small radius which defines two funnels that may define the initial jet shape (Yuan and Narayan 2014). (Jets are also formed by pulsars like the Crab pulsar, and here the hoop stress of the toroidal magnetic field downstream of the termination shock may be responsible for the confinement (Komissarov and Lyubarsky 2003).) There are actually three accretion regimes. At low mass supply rates the electrons may be much cooler than the ions and unable to cool the gas on an inflow timescale. Conversely, at a high mass supply rate, the gas can radiate but the Thomson opacity is so high that the photons are convected inward faster than they can escape outward. It is only at an intermediate mass supply rate that a thin accretion disk will form. On quite general grounds, the low and high supply regimes require powerful winds to carry off the energy that is released during accretion (Blandford and Begelman 1999).

2.4 Magnetars

A minority of neutron stars, called *magnetars* have surface field strengths in the 10-100 GT range over two orders of magnitude more than typical radio or X-ray pulsars (see Kaspi and Beloborodov 2017, for a review). They are found to be rotating with periods $\sim 1 - 10\,$s range but could have been borne with millisecond periods and, if so, they would be strong candidates for the prime-movers of GRBs. Magnetars show dramatic flares (Evans et al 1980; Hurley et al 1999, 2005; Mereghetti et al 2005; Boggs et al 2007) which are likely to be caused by magnetic instability associated with either the crust or the magnetosphere (Thompson and Duncan 1995, 1996). (The energy release is far too much to be derived from rotation.) The emission sites are likely to be electromagnetically-dominated. The

underlying electromagnetic instability may involve rapid, relativistic reconnection of flux tubes, or may be simple untangling with small changes of magnetic helicity. Shocks and non-relativistic reconnection may account for the acceleration needed for more slowly varying emission from these sources.

3 General Principles

3.1 Steady vs Impulsive Acceleration

We have emphasized the rapid variability in these sources because it provides an important clue as to the underlying physical conditions (Begelman et al 2008). However, much of the power is associated with slowly varying source components and extreme particle acceleration is not required. Nonetheless, it is still the case that the radiative efficiency must be high which implies that the associated cooling timescale should be short compared with the expansion timescale in an outflow and the timescales for other non-radiative losses.

The most commonly invoked means for converting large scale electromagnetic energy into high energy particles and radiation is through magnetic reconnection (Biskamp 2000; Priest and Forbes 2000). There has been much effort devoted to understanding nonrelativistic reconnection especially in the context of space and solar physics and also for Tokamaks. The basic idea is that magnetic field is convected by the flow, more or less incompressibly with little dissipation almost everywhere. However, small regions are created where the field reverses abruptly and the current density increases until sufficient dissipation is produced to allow the magnetic field lines to "exchange partners", or "reconnect", with a loss of magnetic energy. It is generally the case that surprisingly energetic particles are produced but with low efficiency. Reconnection need not be steady; various instabilities, like the *tearing mode*, can occur (e.g., Furth et al 1963). Also the microscopic description requires the tensor character of the electrical conductivity to be included (e.g., Wang et al 2000). In §3.2, we will discuss some basic particle acceleration mechanisms in reconnection.

Relativistic reconnection is now being simulated and is clearly much more promising as an agency of extreme particle acceleration (e.g. Zenitani and Hoshino 2001; Guo et al 2014; Sironi and Spitkovsky 2014; Werner et al 2016). However, non-relativistic reconnection may be a slow process, and as such would be better suited to steady acceleration to modest energy, rather than the extreme, "impulsive" acceleration needed for the the most dramatic flares.

3.2 Basic Particle Acceleration in Reconnection

There has been much simulation study of the particle acceleration in magnetic reconnection, and several different acceleration processes operating in various regions in the multi-scale reconnection system have been proposed. Since the dominant electric field responsible for particle acceleration is the inductive electric field during time evolution of reconnection, the magnetic diffusion region, which coincides with the so-called X-type region, would be the principal particle acceleration site. As shown in Figure 1 (A), the charged particles, whose motions are described by

Speiser (meandering) motion (Speiser 1965), can almost directly resonate with the inductive electric field and can be quickly accelerated in the diffusion region where the magnetic field is weak. This acceleration may be almost free from synchrotron radiation loss. However, the volume size of the X-type region is small for the standard *Petschek* reconnection model associated with a pair of slow mode shocks (Petschek 1964), and the total energy release rate would not be necessarily large. For the case of *Sweet-Parker* reconnection with an elongated diffusion region in plasma sheet (Parker 1963), there may be enough volume for direct acceleration in the meandering motion by the electric field, but the magnitude of the electric field is weak compared to Petschek reconnection, because the dimensionless reconnection rate in the Sweet-Parker model is estimated as $1/\sqrt{R_m}$, which should be contrasted with the reconnection rate in Petschek model $\sim 1/\ln(R_m)$, where $R_m = LV_A/\eta$ is the magnetic Reynolds number based on the inflow Alfvén velocity V_A, which is also frequently referred to as Lundquist number, L is the length of the reconnection region and η is the magnetic diffusivity.
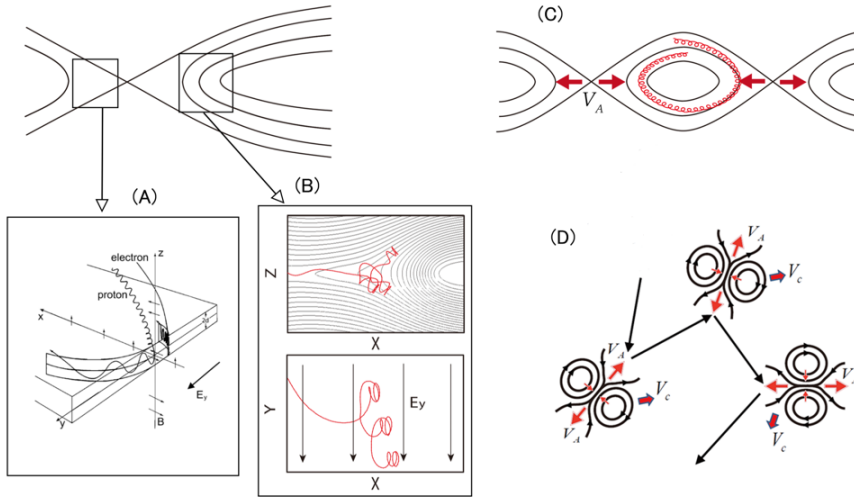

Fig. 1 Typical particle orbits accelerated during magnetic reconnection. (A) *Speiser* motion/meandering motion, adapted from (Speiser 1965). Particles can get accelerated during the meandering/bouncing motion along the electric field, under the anti-parallel magnetic field B_x, (B) the gradient/curvature B drift motion in the magnetic field pileup region, (C) the trapped particles in the shrinking magnetic islands, (D) the stochastic Fermi acceleration in multiple magnetic islands.

In addition to the *Speiser* motion in the diffusion region, particles can be accelerated in the pileup magnetic field region produced by compression of the reconnection outflow. The collision of the reconnection outflow emanating from the diffusion region with the pre-existing plasma at rest will produce the pileup

region associated with a large jump of magnetic field. Figure 1 (B) shows that the ∇B and/or curvature B drift motion for ions/electrons, which is parallel/anti-parallel to the inductive electric field, contributes to the energization (Hoshino et al 2001). If the particles are magnetized and their gyro-radii are small compared with the scale height of the pileup magnetic field, the first adiabatic invariant $p_\perp^2/B$ is conserved, and a large energy gain can be expected due to the large jump of the magnetic field intensity.

Not only the X-type and the B pileup regions in the single reconnection site, but magnetic islands surrounded by the loop-like magnetic field lines, which situation can happen for multiple reconnection/tearing mode instability in a long current sheet, can invoke particle energization, shown in Figure 1 (C). Because of the shrinking magnetic field lines bounded by two X-type regions at each end, the particles trapped by the magnetic island can gain energy by reflection from both ends of the contracting magnetic field line (Drake et al 2006). The energy gain in this Fermi acceleration process can be estimated from the conservation of the second adiabatic invariant $p_\parallel L$, where L is the loop length of the magnetic island. However, as being energized by the contracting magnetic field line, the particles will escape from the island if their gyro radii become comparable with the size of the island and the particle acceleration will cease.

However, it is possible that high energy particles can be further accelerated in a much larger plasma environment with many magnetic islands. By analogy to the original Fermi acceleration model, where particles gain energy stochastically during head-on and head-tail collisions of particles with many magnetic clouds, let us replace the magnetic clouds with magnetic islands, as shown in Figure 1 (D). In the original Fermi acceleration, the increase in particle energy is known to be of second order in V_c/c, where V_c is the speed of random motion of magnetic clouds. However, if there are many magnetic islands with the Alfvénic plasma outflow, it is suggested that the particles can preferentially interact with the reconnection outflow region, because the energetic particles have a tendency to be situated outside the magnetic island during acceleration. As a result, the increase in energy becomes first order of V_A/c, where V_A is the Alfvén speed (Hoshino 2012).

Regardless of the acceleration mechanisms in details, another key issue for a rapid magnetic energy dissipation and particle acceleration is how the large electric field is generated during reconnection. The average electric field in the reconnection system is basically determined by $V \times B/c$ induced by the inflow and outflow motions, and roughly speaking the outflow speed can reach the Alfvén speed for both non-relativistic and relativistic reconnections. Since the Alfvén speed is given by $V_A = c\sqrt{\sigma/(\sigma+1)}$, the fast reconnection flow and the large electric field can be realized in a strong magnetized plasma with a large σ value. The spontaneous vs driven reconnection is another key issue to control the reconnection rate. It is known that small but finite Poynting flux injection from the inflow boundary into the system can drive a fast reconnection for both linear and nonlinear stages. While the linear growth rate for the spontaneous tearing mode is proportional to $R_m^{-3/5}$ (Furth et al 1963), the growth rate for the driven case is $R_m^{-1/3}$ (Horton and Tajima 1988). The enhancement of the reconnection rate can be also found in the double tearing mode, which is characterized by the presence of two (or more) tearing current sheets whose surfaces are attached to each other. The reason of enhancement of reconnection rate is simply because the surface can share the

inflow and outflow boundary condition for two tearing islands, which is the same situation as arises in driven reconnection.

3.3 Pairs vs Hadrons

There has been much discussion of the nature of the positive charge carriers especially in jets. Are they positrons or protons? Given the large EMFs generated, the former are readily created through γ–γ or even γ-B processes although this may be balanced by pair annihilation at the base of the jet. However hadrons are likely to be incorporated into the flow through entrainment from the surrounding medium, which might comprise gas accreting at high latitude, gas clouds in the interstellar medium, a thick, confining torus or an outflowing wind. Probably all four possibilities are relevant. It may be that this is the explanation for the famous Fanaroff and Riley (1974) dichotomy of double radio sources, with the low power, Type 1 sources being identified with jets that are efficiently decelerated by their surrounding and Type 2 sources containing jets that are not slowed down. If the proton density is high, shocks are likely to be very important particle accelerators but conditions will then not be propitious for extreme acceleration/magnetoluminescence.

3.4 Emission Mechanisms

Although we surely trust the physics of the underlying radiative processes, we are not completely confident that we understand which of them operates and where. The "Bactrian" (two-humped) spectrum characteristic of blazars has been commonly interpreted as a two process — synchrotron and Compton — emission from a single, homogeneous source. However, jets are observed to radiate all along their lengths and it seems more likely that both humps comprise emission from different radii. Interestingly, there is a maximum synchrotron photon energy that can be radiated in a simple electromagnetic source. If we balance the rate of energy gain $\sim eEc$ by the radiative loss and impose the condition $E \lesssim B$, then the maximum photon energy is found to be $\sim m_e c^2/\alpha$, where α is the fine structure constant. This is $\sim 70\,\mathrm{MeV}$.

It is common to distinguish two types of Compton radiation with externally produced photons dominating in the FSRQs and internal synchrotron photons dominating in the BLLs. Again, it seems more reasonable to suppose that both options are exercised along the jet.

The self-absorbed synchrotron radio emission seen from jets, known as the *core*, sometimes seems to vary so rapidly that the emission mechanism may have to be coherent, perhaps a cyclotron maser (Begelman et al 2005). An important constraint is that the radio waves have to avoid absorption due to the induced Compton effect or stimulated Raman scattering which sets an upper limit on the electron column density along the line of sight (Levinson and Blandford 1995).

There are more options if hadrons are present. There have been several suggestions that the γ-rays are produced as a consequence of pion production following proton-proton collisions. The neutral pions decay efficiently into gamma rays. However, more of the energy goes into charged pions where the decays involve muon and electron neutrinos and may produce particles that are insufficiently energetic

to radiate efficiently. A variation which deserves more attention is for a proton be accelerated to very high energy so that it can photo-produce electron-positron pairs which quickly radiate by the synchrotron process into the "Compton" hump at energies above the conventional synchrotron limit. This might be important in a high radiation density environment in a GRB or a quasar.

3.5 Relativistic Beaming

Doppler beaming is an essential feature of electromagnetic flows as the characteristic signal speed is necessarily relativistic. The easiest way to handle this is to introduce a *Doppler factor* $\mathcal{D} = [\Gamma(1 - \mathbf{V} \cdot \mathbf{n}/c)]^{-1}$, where $\Gamma = (1 - V^2/c^2)^{-1/2}$, for Lorentz transformation from a (primed) frame in which we can evaluate the emissivity $j'_{\nu'\Omega'}(\nu', \mathbf{n}')$ and the absorption coefficient $\kappa'(\nu', \mathbf{n}')$. $\mathbf{V}$ is the velocity of the primed frame in the frame of a distant, though not cosmologically distant, observer along a direction $\mathbf{n}$. Primed frame quantites are transformed into observer frame quantities according to $dt = \mathcal{D}^{-1}dt'$, $\nu = \mathcal{D}\nu'$, $\mathbf{n}' = \mathcal{D}\mathbf{n} - \Gamma(\mathcal{D} + 1)\mathbf{n}/(\Gamma + 1)$, $j_{\nu\Omega}(\nu, \mathbf{n}) = \mathcal{D}^2 j_{\nu'\Omega'}(\nu', \mathbf{n}')$, $\kappa_{\nu\Omega}(\nu, \mathbf{n}) = \mathcal{D}^{-1}\kappa_{\nu'\Omega'}(\nu', \mathbf{n}')$ (e.g., Blandford and Königl 1979). The intensity, which transforms according to $I_{\nu\Omega}(\nu, \mathbf{n}) = \mathcal{D}^3 I_{\nu'\Omega'}(\nu', \mathbf{n}')$, is best considered in the observer frame and can be corrected for cosmological expansion if appropriate. For a source that is beamed towards us, it is a good start to approximate these formulae by setting $\mathcal{D} \sim \Gamma$.

With the increasing sophistication of simulations of electromagnetic sources, it is worth carrying out more careful radiative transfer calculations. These are best prosecuted in the unprimed, observer frame, transforming the emissivity and absorption coefficient into this frame.

4 Global Issues

4.1 Voltages and Currents

Before discussing details, it is helpful to consider the global energy balance in a relativistic, electromagnetic source. In the most simple-minded model of a spinning conductor with angular frequency Ω and threaded by magnetic flux Φ, the potential difference generated is $V_{\text{eff}} \sim \Omega\Phi/2\pi$. There will be a current flow I_{eff} outside the body and the effective impedance will be roughly that of free space $Z_{\text{eff}} \sim 100\,\Omega$ so that $I_{\text{eff}} \sim V_{\text{eff}}/Z_{\text{eff}}$. The power that can be effectively dissipated as particle acceleration is then $L_{\text{eff}} \sim V_{\text{eff}}I_{\text{eff}} \sim \Omega^2\Phi^2/4\pi^2 Z_{\text{eff}}$. In the case of a magnetar where the energy release is gravitational, Ω should be replacedby Ω_{eff} the reciprocal of the characteristic timescale associated with the release of seismic energy.

Let us give some examples. For the Crab pulsar, $V_{\text{eff}} \sim 50\,\text{PV} \sim 5 \times 10^{16}\,\text{V}$ and $L_{\text{eff}} \sim 3 \times 10^{31}\,\text{W}$, comparable with the bolometric luminosity of the Crab Nebula. For a quasar like 3C279, $V_{\text{eff}} \sim 300\,\text{EV} \sim 3 \times 10^{20}\,\text{V}$ and $L_{\text{eff}} \sim 10^{39}\,\text{W}$ and for a powerful GRB, $V_{\text{eff}} \sim 100\,\text{ZV} \sim 10^{23}\,\text{V}$ and $L_{\text{eff}} \sim 10^{44}\,\text{W}$. Note that there is sufficient potential difference to accelerate Ultra High Energy Cosmic Rays (UHECR) in powerful AGN though whether or not these particles can escape without suffering catastrophic photopion production loss is debatable. Newly born

magnetars, with 10^{11} T surface magnetic field and an initial spin rate close to the centrifugal breakup limit, could generate an EMF $V_{\text{eff}} \sim 10\,\text{ZV} \sim 10^{22}\,\text{V}$; they, too, have been considered as viable accelerators for UHECR (Arons 2003).

A very simple effective circuit description raises the question of where do these currents close. If this is closeby, the flow becomes gas dynamical and remote acceleration is likely to be associated with shocks and shear flows. Alternatively, the current may persist to the observed extremity of the source, for example the hot spots associated with a powerful double radio source. In this case, the processes discussed here are likely to be relevant to most of the emission.

4.2 Flow of Flux

The voltage V_{eff}, measured in V is also the flow of magnetic flux measured in Wb s^{-1}. If as is the case with a pulsar wind nebula, the flux is confined within a volume that is expanding much slower than the speed of light then the flux must be dissipated at almost the rate at which is supplied. Particle acceleration in one form or another is inevitable. (If this did not happen and the walls were perfect conductors, then the electromagnetic field would react back on the source.) The only questions are where does it occur and what are the resulting particle energy distributions. For an axisymmetric rotating source, the two most promising possibilities are the symmetry axis where the polar current will be concentrated and along the path of the return current, specifically along the equatorial plane in a pulsar wind nebula and along the jet walls in the case of AGN jets. There is observational evidence for both of these (Hester et al 1995; Weisskopf et al 2000; Reid et al 1989).

5 Relativistic MHD Description

5.1 Knots and Tangles

Although there may be some validity to describing the electromagnetic field under the force-free approximation close to the source, the inertia of the plasma is likely to become significant quite quickly and relativistic MHD will be the preferred fluid description although we have little understanding of how the particle density builds up and is regulated. Nonetheless it is reasonable to expect that MHD instabilities will break any axisymmetry and lead to the formation of current sheets. As is observed in the solar corona, "hairy" magnetic ropes are likely to form, twisted by field-parallel (zero-stress) current. The extent to which this is a fair description of these magnetically dominated sources is unknown but if we adopt it, it is easy to believe that the writhing *magnetic ropes* can become both tangled and knotted.

The distinction is important. A knot, which contributes to the magnetic helicity $H = \int dV\, \mathbf{A} \cdot \mathbf{B}$ (Moffatt 1978; Bellan 2000), is topologically distinct from a tangle or "unknot" (Fig. 2). If the magnetic field that is created by the prime mover is required to evolve according to the precepts of perfect MHD, it will remain unknotted. Even if H were non-zero initially, it would decrease in inverse proportion to the scale size of the flow. However, if magnetic ropes form, it is an inevitable consequence of instability in these outflows that there will be places where they
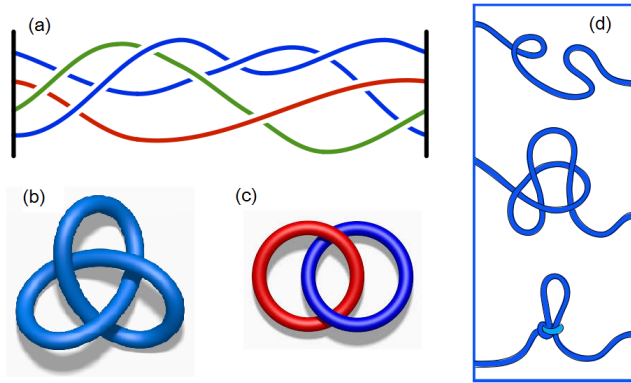
Fig. 2 An illustration of topologies the magnetic "ropes" may take. (a) Braid. (b) Knot. (c) Link. (d) Hitch, which is topologically equivalent to a straight line.

will be pulled or pressed against one another. Reconnection of pairs of ropes at unrelated locations seems to be inevitable with an overall release of energy through relaxation of magnetic tension and transverse expansion. The knots that are then created topologically will be initially quite loose but are likely to tighten under the action of magnetic tension with the passage of time. Additional instances of forced reconnection will resolve these knots, leading to further energy release and particle acceleration. (Knots are very important in the history of physics as their *aetherial* expression was once the most popular model of atoms (Tait 1907). They have also played a prominent role in modern field theory.)

However, it also seems to be quite likely that tangles of individual ropes will develop and tighten into *slip knots* or *hitches* that may be resolved without large-scale reconnection simply through an increase in magnetic tension. As with conventional ropes the ease with which this can happen depends upon the surface friction. In the case of magnetic ropes this will depend upon small-scale electromagnetic stresses associated with the "hair"—wandering field lines near the boundary of the flux ropes. If the friction is large, then large tangles with large latent energy can be created.

From a particle acceleration standpoint, tangles can untangle at effectively the speed of light in a relativistic source and can be responsible for the flares; knots require reconnection, which may be slower to resolve, and may be responsible for the higher power, steady emission.

5.2 Sheets, Shocks and Caustics

Many of the relativistic sources that we have been discussing, such as blazar jets, are observed to be expanding relativistically. Others, such as pulsar wind nebulae, have relativistic sound speeds and can therefore sustain internal relativistic motions. Doppler boosting with Lorentz factor Γ, as summarized in Sec. 3.4, is therefore likely to be present and to contribute to the observed flux. If we idealize the source as a sphere moving with a single velocity, then we may see variation as the source expands in its own reference frame. Alternatively, the velocity may turn through an angle $\gtrsim \Gamma^{-1}$ and this will produce a roughly symmetric pulse.

Parallel acceleration should produce an asymmetric pulse. Changes in the optical depth at either radio or γ-ray energy can also produce rapid variation.

However, there are additional possibilities if the emission comes from a surface, such as a current sheet or a shock front that is moving ultrarelativistically. An element of the surface may beam the synchrotron or Compton radiation in a narrow cone about its direction of motion. (Among several factors which could complicate a detailed model, the speed of the emitting surface might differ from the speed of the emitting plasma, as happens in a shock front. In addition the electrons and positrons might be carrying a current and moving with different speeds.) Now, for a generic, corrugated surface, the mapping from the moving surface onto a distant sphere might be many to one which can lead to the formation of caustics (cf, Lyutikov et al 2012). The simplest generic caustic is a *fold* which produces an asymmetric flux variation $\propto |t - t_0|^{-1/2}$ before or after the time t_0 when a pair of images either disappears or appears. Effects such as these could enhance the observed variability from sources where extreme particle acceleration might be taking place.

5.3 MHD Simulations

In recent years much progress has been made in relativistic MHD simulations to address the plasma dynamics in pulsar wind nebulae, the formation, propagation and acceleration of jets from black holes/neutron stars, the propagation of shocks/blast waves in GRBs, and so on. We are gradually gaining a reasonable picture of how the magnetized outflow from the engine shapes its environment, as described in many other chapters of this book. Meanwhile, a lot more work is needed to understand the actual dissipation process. Here, as a good starting point, we can focus on a local region in the plasma outflow that has a tangled magnetic field topology, to see whether a rapid conversion of electromagnetic energy to particle kinetic energy can occur.

As one example, East et al (2015) considered a family of force-free equilibria in a 3D periodic Cartesian box. These configurations have the topology of multiple flux ropes packed in a complex manner. They are solutions to the force-free equation $\nabla \times \boldsymbol{B} = \lambda \boldsymbol{B}$, where λ is a constant throughout the space, so each of them has a single characteristic wavelength (Chandrasekhar and Kendall 1957; Moffatt 1986; Rosenbluth and Bussac 1979; Bellan 2000):

$$\boldsymbol{B} = \sum_{|\boldsymbol{k}|=|\lambda|} \hat{n}_{\boldsymbol{k}} \times \nabla \chi_{\boldsymbol{k}} + \frac{1}{\lambda} \nabla \times (\hat{n}_{\boldsymbol{k}} \times \nabla \chi_{\boldsymbol{k}}) \tag{1}$$

Here $\chi_{\boldsymbol{k}}$ is the solution to the scalar Helmholtz equation $\nabla^2 \chi + \lambda^2 \chi = 0$, $|\boldsymbol{k}| = \lambda$, and $\hat{n}_{\boldsymbol{k}}$ is a constant unit vector. At a fixed total helicity H, if a configuration has a shorter wavelength, namely, it contains a larger number of smaller flux ropes, then its total magnetic energy is higher.

Constant-λ force-free configurations have historical importance, because Taylor's conjecture suggests that a closed, magnetically dominated plasma tends to relax to lower energies while conserving the total helicity, and the relaxed state is just one such constant-λ configuration (Taylor 1974, 1986).

MHD/force-free simulations by East et al (2015) found that, typically, the shorter wavelength equilibria are unstable to ideal MHD modes; the instability grows on Alfvén crossing time scales, and in the nonlinear regime the system goes through a turbulent relaxation process, dissipating a finite amount of energy within just one dynamic time scale. Eventually the plasma settles into the longest possible wavelength.
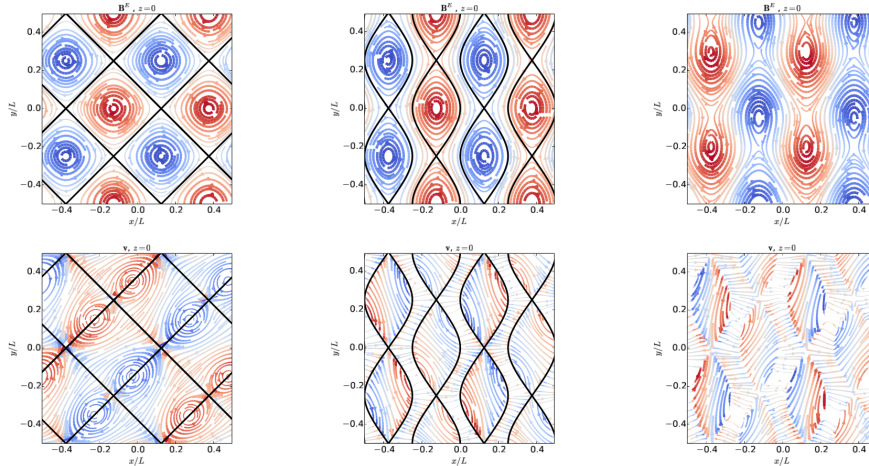

Fig. 3 Streamlines of the magnetic field in the initial force-free equilibria for three different examples (top row), and the corresponding velocity field $\boldsymbol{v} = \boldsymbol{E} \times \boldsymbol{B}/B^2$ of the maximally growing unstable mode found from the force-free simulations (bottom row) (from East et al 2015). The first two equilibria are 2D while the third one is 3D. All plots show streamlines on the $z = 0$ plane. The color indicates the perpendicular vector component with red and blue representing, respectively, out of the page and into the page. The thickness of the streamline is proportional to the vector magnitude. The black lines indicate the location of the separatrices in the equilibrium solutions.

Figure 3 shows a few examples of the force-free equilibria and the corresponding maximally growing unstable mode. It suggests that the instability can be viewed as shearing and merging of the flux ropes. The velocity field appears to have non-smooth features, reminiscent of spontaneous current sheets that occur at the flux tube boundaries. In Figure 4, it is shown that different volume averaged magnetization values $\sigma \equiv \langle B^2/(4\pi w)\rangle$ (where w is the plasma enthalpy) give the same intermediate and final energy levels, consistent with conservation of magnetic helicity. The amount of magnetic energy dissipated during the evolution thus corresponds to the *free* magnetic energy, defined as the energy difference between the initial configuration and the ground state (longest wavelength state), compared at the same helicity.

These systematic numerical investigations suggest that, in general, the generic short wavelength, constant-λ force-free states in 3D periodic boxes are unstable; the instability is characterized by an exponentially growing electric field in the linear phase, and eventually leads to current sheet formation where significant
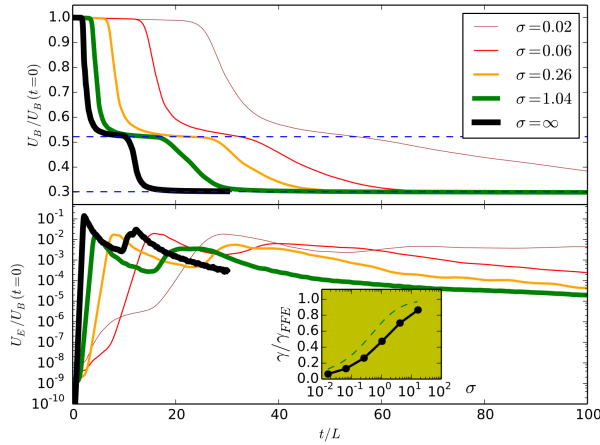
Fig. 4 A comparison of the decay of an $\lambda^2 = 11$ equilibrium in simulations with different values of volume averaged magnetization $\sigma \equiv \langle B^2/(4\pi w) \rangle$, where w is the plasma enthalpy (from East et al 2015). Shown is the magnetic energy (top) and kinetic/electric field energy (bottom). The horizontal dashed lines in the top panel indicate the magnetic energy of $\lambda^2 = 3$ and $\lambda^2 = 1$ states with the same helicity. The bottom inset shows the linear growth rate γ measured for runs having different magnetization parameters, along with the Alfvén speed (dashed line) for comparison.

amount of the free magnetic energy is dissipated within just a single light crossing time.

Lyutikov et al (2016b) also studied independently a subset of the force-free equilibria — 2D "ABC" field (after Arnol'd (1965), Beltrami (1902), Childress (1970), e.g. Moffatt (1986))— to explore the viability of impulsive magnetic energy release. They reach the same conclusion that these configurations are unstable to ideal modes and collapse over dynamic time scales. They show that when the structures are initially compressed or sheared (driven system), the development of the instability can be accelerated.

Although the above plasma configurations are quite artificial, they teach us a lot about the generic behavior of highly magnetized, relativistic plasmas. Similarly complex, current-carrying plasma states with plenty of free energy may form in the pulsar wind (e.g., Zrake 2016), or downstream of the oblique termination shock in PWN where the magnetization is still high (Lyutikov et al 2016b), and also in jets due to kink instability. The insights gained here are instructive to envisage the possibility of catastrophic conversion of large scale electromagnetic energy into particle kinetic energy.

6 Kinetic Description

6.1 Distribution Function

In order to understand what are the underlying dissipation mechanisms, how the released electromagnetic energy is partitioned among the particles, and what emission the accelerated particles produce, we need to follow the evolution of par-

ticle distribution in phase space. For relativistic plasma, we use the following covariant definition of distribution function over the 6-dimensional phase space: $F(\boldsymbol{x}, \boldsymbol{u}, t) = dN/(d^3x\, d^3u)$, where $\boldsymbol{x}$ is the position and $\boldsymbol{u}$ is the spatial part of the 4-velocity of the particles. In many of the aforementioned astrophysical environments, the plasma is collisionless, meaning that the Coulomb collisional time scale is much longer than the relevant dynamic time scales. The evolution of the distribution function for each species F_s then follows the collisionless Boltzmann equation, or Vlasov equation:

$$\frac{\partial F_s}{\partial t} + \nabla_{\boldsymbol{x}} \cdot (\boldsymbol{v} F_s) + \nabla_{\boldsymbol{u}} \cdot (\frac{d\boldsymbol{u}}{dt} F_s) = 0, \tag{2}$$

where $\boldsymbol{v} = \boldsymbol{u}/\gamma$ is the 3-velocity, $\gamma = \sqrt{1 + u^2/c^2}$ is particle Lorentz factor, and the acceleration of individual particles is determined by

$$m_s \frac{d\boldsymbol{u}}{dt} = q_s (\boldsymbol{E} + \frac{\boldsymbol{v}}{c} \times \boldsymbol{B}). \tag{3}$$

Other forces, like radiation reaction force, can be included as well. The electromagnetic field determines the motion of particles, at the same time its evolution is determined by the charge and current density provided by the particles

$$\rho = \sum_s q_s \int F_s d^3u, \tag{4}$$

$$\mathbf{J} = \sum_s q_s \int F_s \frac{\mathbf{u}}{\gamma} d^3u, \tag{5}$$

This is a complex system to solve. The current state-of-the-art technique is Particle-In-Cell (PIC) simulations, which exploit a fixed spatial grid to evolve the electromagnetic field, while the particle distribution function is sampled by a large number of particles. PIC method has been successfully applied to study collisionless shocks (e.g., Spitkovsky 2008; Sironi and Spitkovsky 2009, 2011b,a), plane current sheet reconnection (e.g. Kagan et al 2015), magneto-rotational instability (MRI, e.g. Hoshino 2015; Riquelme et al 2012), global pulsar magnetospheres (e.g., Chen and Beloborodov 2014; Belyaev 2015; Cerutti et al 2015; Philippov et al 2015), and so on, with very fruitful outcomes.

   In the following, we summarize some key results from PIC simulations of the rapid energy release processes mentioned in §5.3. These simple yet instructive models serve as a good testbed for understanding the details of electromagnetic dissipation, particle acceleration and high energy radiation.

6.2 Relaxation of force-free equilibria

A few groups, including Nalewajko et al (2016); Lyutikov et al (2016b); Yuan et al (2016), have carried out 2D PIC simulations of the unstable force-free equilibria. In PIC simulations, the overall evolution of the system is quite similar to MHD/force-free simulations (Fig. 5): initially the ideal instability grows on Alfvén wave crossing time scales, producing current layers at the interface of merging flux ropes—this is consistent with the X-point collapse scenario for current sheet formation. The current layers are short-lived though, and the system enters a turbulent

relaxation phase, eventually settling into the longest wavelength configuration, with almost all the available magnetic free energy converted to particle kinetic energy. The total helicity is also approximately conserved in PIC simulations.
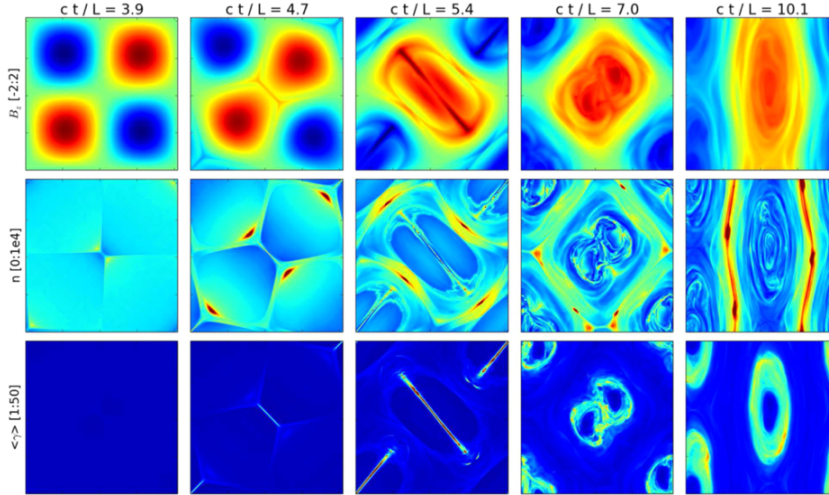

Fig. 5 Snapshots from a 2D PIC simulation of one of the lowest order unstable force-free equilibria (from Nalewajko et al 2016). Top panels: out of plane component of the magnetic field (there is also in-plane magnetic field); middle panels: number density n of electrons and positrons; bottom panels: average Lorentz factor $\langle\gamma\rangle$ of electrons and positrons.

However, PIC simulations show richer structures during the evolution, especially the kinetic effect on current sheet formation — plasmoid generation during the thinning and stretching of the current sheets, and magnetic reconnection at these sheets. It is observed that the thickness of the current layer at its maximal stretch scales as the Larmor radius $r_{\mathrm{L, hot}}$ of the high energy electrons accelerated/heated by reconnection. The reconnection rate is measured to be in the range $v_{\mathrm{rec}}/c \sim 0.2-0.5$, which increases with the magnetization and saturates at around 0.5 at high magnetization limit (Lyutikov et al 2016b). There appear to be two different phases of particle acceleration in the whole process. The first phase corresponds to the formation of the first, biggest current layers where reconnection of in-plane field takes place. $\boldsymbol{E} \cdot \boldsymbol{B} \neq 0$ in the current sheet, with the reconnection electric field $\boldsymbol{E}$ directed primarily out of plane, which causes run-away particle acceleration in the current sheet. This acceleration is fast, producing a relatively hard, high energy component in the particle distribution (Fig. 6). The second phase follows when the first current layers dissolve and the system evolves chaotically; the oscillating field structures scatter the particles around; there is evidence of second order Fermi acceleration smoothing out the high energy component to a softer power law, also bulk heating that increases the temperature of the thermal component.

It turns out that the particle acceleration efficiency depends on the mean magnetization of the configuration, in a similar fashion as plane current sheet recon-
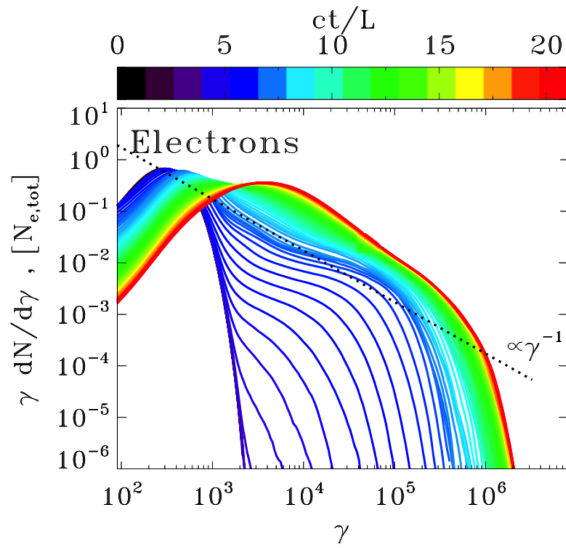
Fig. 6 Particle spectrum from a 2D PIC simulation of ABC instability with initial temperature $kT/mc^2 = 10^2$, in-plane magnetization $\sigma_{\rm in} = 42$ (defined with respect to the enthalpy w), and $L = 126r_{\rm L,\,hot}$, where L is the linear size of one flux tube, $r_{\rm L,\,hot}$ is the Larmor radius of high energy electrons heated/accelerated by reconnection (from Lyutikov et al 2016b). The spectrum during the initial phase of rapid acceleration (blue to cyan lines) can be harder than $\gamma dN/d\gamma \propto \gamma^{-1}$ (compare with the dotted line), as indeed required by the observations of the Crab flares.

nection scenarios (Guo et al 2014; Sironi and Spitkovsky 2014; Werner et al 2016). The particle spectrum gets harder as the mean magnetization increases; both the non-thermal particle fraction and the maximum particle energy increase with the magnetization (Lyutikov et al 2016b; Nalewajko et al 2016).

When we look at the synchrotron radiation signals from this evolving plasma, we find that, since the highest energy particles are first accelerated in the current layers by the parallel electric field, they do not radiate much when they are inside the sheet, because the curvature of their trajectory is small (despite the presence of guide field in the current layer). Most of the radiation is produced when particles are ejected from the current layers—their trajectories start to bend significantly in the ambient magnetic field which changes direction at the end of the current layer (Fig. 7). Such a separation of acceleration site and radiative loss site could in principle facilitate acceleration beyond the synchrotron radiation reaction limit (Uzdensky et al 2011). Fast variability of observed photon flux can be produced when compact plasmoids that contain high energy particles are ejected from the ends of the current layers and get destroyed. These give beamed radiation. An observer sees high intensity radiation when the beam happens to be aligned with the line of sight. This is a picture similar to the kinetic beaming seen in plane current sheet reconnection simulations (Cerutti et al 2013, 2014). As a result, the high energy radiation is much more variable than the low energy radiation, and these emission peaks are accompanied by an increase in the polarization degree and rapid change of polarization angle in the high energy band (Yuan et al 2016). The variability timescale is determined by the spatial extent of the emitting structure,
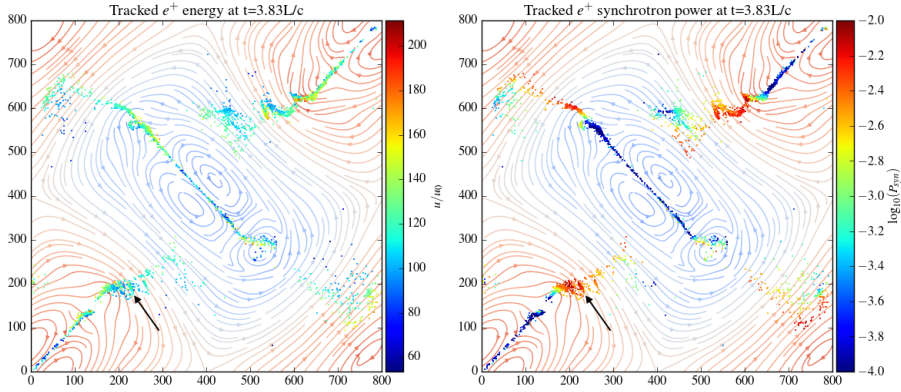
Fig. 7 A snapshot of the location of tracked high energy positrons, plotted over the instantaneous field structure (Yuan et al 2016). In the left panel, the particles are color-coded by their energy while in the right panel they are color-coded by the synchrotron power. The arrows locate the ejection of plasmoids.

e.g. the plasmoids, thus can be much shorter than the light crossing time of the region that collapses.

6.3 X-point collapse

As we have discussed above, the initial rapid phase of particle acceleration in 2D PIC simulations of unstable force-free equilibria occurs at the current sheets created in between flux ropes. There, the evolution of the field line geometry resembles the X-point collapse studied by Syrovatsky in the non-relativistic regime (Syrovatskii 1966; Imshennik and Syrovatskiĭ 1967) and by Lyutikov et al (2016b) in the relativistic regime. The vector potential for the X-point geometry is $A_z = -1/2\left(x^2/a(t)^2 - y^2/b(t)^2\right)$, where $b(t) = \lambda/a(t)$. The unstressed case of $\lambda = 1$ is stable. Below, we present results for the stressed case $\lambda = 1/\sqrt{2}$, for magnetizations $\sigma \gg 1$ and magnetic fields initialized only in the simulation plane (i.e., in the absence of the so-called "guide field"). As shown in Fig. 8, the collapse proceeds self-similarly: the macroscopic distribution of E^2/B^2 (and hence that of the drift velocity) at later times is a scaled copy of that at previous times, with the overall length scale increasing linearly with time (at the speed of light). This implies that the reconnection rate over the whole configurations remains fixed in time (and we find that for highly magnetized plasmas, the reconnection rate v_{rec} approaches the speed of light on macroscopic scales).

Interestingly, the electric field increases linearly with time. This is ultimately a manifestation of the self-similar macroscopic evolution of the system. Indeed, since in the initial configuration the magnetic field strength grows linearly with distance from the origin (i.e., the center of the X-point) and the current sheet size grows linearly with time, the mean magnetic and electric fields in the volume surrounding the current sheet must also grow linearly, with their scaled distributions
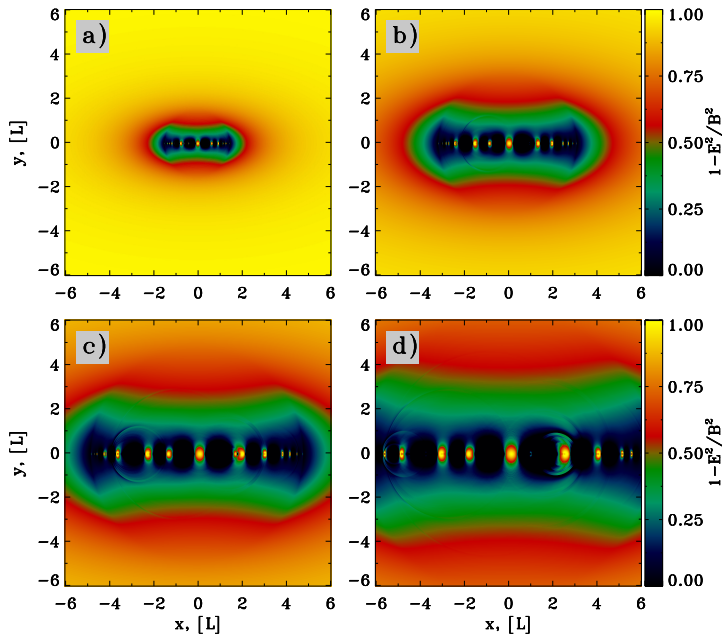
Fig. 8 Late time evolution of the X-point collapse in PIC simulations with zero guide field (Lyutikov et al 2016b), for $\sigma = 4 \times 10^4$ (the magnetization is measured in the initial setup at unit distance from the center). The plots show the quantity $1 - E^2/B^2$ (strictly speaking, we plot $\max[0, 1 - E^2/B^2]$) at $ct/L = 1.5, 3, 4.5, 6$, from panel (a) to (d).

unchanged. The temporal evolution of the electric field has a direct impact on the maximum particle energy. Quite generally, its time evolution will be

$$\gamma_{\max} \propto Et \propto v_{\mathrm{rec}}Bt \qquad (6)$$

Since both E and B in the reconnection region are scaling linearly with time, one expects $\gamma_{\max} \propto t^2$. This is confirmed by Fig. 9, where we follow the trajectories of a number of particles in a simulation with $\sigma = 4 \times 10^2$. The particles are selected such that their Lorentz factor exceeds a given threshold $\gamma_0 = 30$ within the time interval $1.4 \leq ct_0/L \leq 1.7$, as indicated by the vertical dashed lines in the top panel. The temporal evolution of the Lorentz factor of such particles, presented in the top panel for the 30 positrons reaching the highest energies, follows the track $\gamma \propto t^2 - t_0^2$ that is expected from $d\gamma/dt \propto E(t) \propto t$. Here, t_0 is the injection time, when the particle Lorentz factor γ first exceeds the threshold γ_0. The individual histories of single positrons might differ substantially, but overall the top panel of Fig. 9 suggests that the acceleration process is dominated by direct acceleration by the reconnection electric field. We find that the particles presented in the top panel of Fig. 9 are too energetic to be confined within the small-scale plasmoids in the current sheet (see the small scale structures in Fig. 8), so any acceleration mechanism that relies on plasmoid mergers is found to be unimportant, in this setup.

Particle injection into the acceleration process happens in the charge-starved regions where $E > B$, i.e., in the small-scale X-points that separate each pair

of secondary plasmoids in the current sheet. Indeed, for the same particles as in the top panel, the middle panel in Fig. 9 presents their locations at the onset of acceleration with open white circles, superimposed over the 2D plot of $1 - E^2/B^2$ (more precisely, of $\max[0, 1 - E^2/B^2]$). Comparison of the middle panel with the bottom panel shows that particle injection is localized in the vicinity of the small-scale X-points in the current sheet (i.e., the blue regions where $E > B$). Despite occupying a relatively small fraction of the overall volume, such regions are of paramount importance for particle acceleration.

The explosive stage of X-point collapse produces non-thermal tails (in analogy to the relaxation of unstable force-free structures) whose hardness depends on the average magnetization. For sufficiently high magnetizations and vanishing guide field, the non-thermal particle spectrum consists of two components: a low-energy population with soft spectrum, that dominates the number census; and a high-energy population with hard spectrum, that possesses all the properties needed to explain the Crab flares (Lyutikov et al 2016b). The particle distribution is highly anisotropic, with high-energy particles beamed primarily along the direction of the accelerating electric field.

6.4 Merging Lundquist flux ropes

Above, we have described the evolution of unstable force-free configurations (with the ABC geometry being a special case). There are two key features of the preceding model that are specific to the initial set-up: (i) each flux tube carries non-zero poloidal current; (ii) the initial configuration is an unstable equilibrium. However, as we now show, the evolution is generic, regardless of these conditions. Lyutikov et al (2016b) investigated a merger of two flux tubes with zero total current, with MHD and PIC simulations. Thus, two flux tubes are not attracted to each other — at least initially. Here, we present the results for Lundquist's force-free cylinders surrounded by uniform magnetic field,

$$\mathbf{B}_L(r \leq r_{\rm j}) = J_1(r\alpha)\mathbf{e}_\phi + J_0(r\alpha)\mathbf{e}_z \,, \tag{7}$$

Here, J_0, J_1 are Bessel functions of zeroth and first order and the constant $\alpha \simeq 3.8317$ is the first root of J_0. We chose to terminate this solution at the first zero of J_1, which we denote as r_j and hence continue with $B_z = B_z(r_j)$ and $B_\phi = 0$ for $r > r_j$. Thus the total current of the flux tube is zero. As the result, the azimuthal field vanishes at the boundary of the rope, whereas the poloidal one changes sign inside the rope. The evolution is very slow, given the fact that at the contact the reconnecting field vanishes (i.e., the initial configuration is dynamically stable). To speed things up, the ropes are pushed towards each other.

In Fig. 10, we present the 2D pattern of the out-of-plane field B_z (left column) and of the in-plane magnetic energy fraction $\epsilon_{B,\rm in} = (B_x^2 + B_y^2)/8\pi nmc^2$ (right column; with superimposed magnetic field lines), from a PIC simulation with $kT/mc^2 = 10^{-4}$, $\sigma_{\rm in} = 43$ (only defined with the in-plane fields) and $r_{\rm j} = 61\, r_{\rm L,hot}$. As the two magnetic ropes slowly approach, driven by the initial velocity push, reconnection is triggered in the plane $x = 0$, as indicated by the formation and subsequent ejection of small-scale plasmoids. Until $ct/r_{\rm j} \sim 4.5$, the cores of the two islands have not significantly moved (black line in the middle panel of Fig. 11, indicating the $x_{\rm c}$ location of the center of the rightmost island), the reconnection
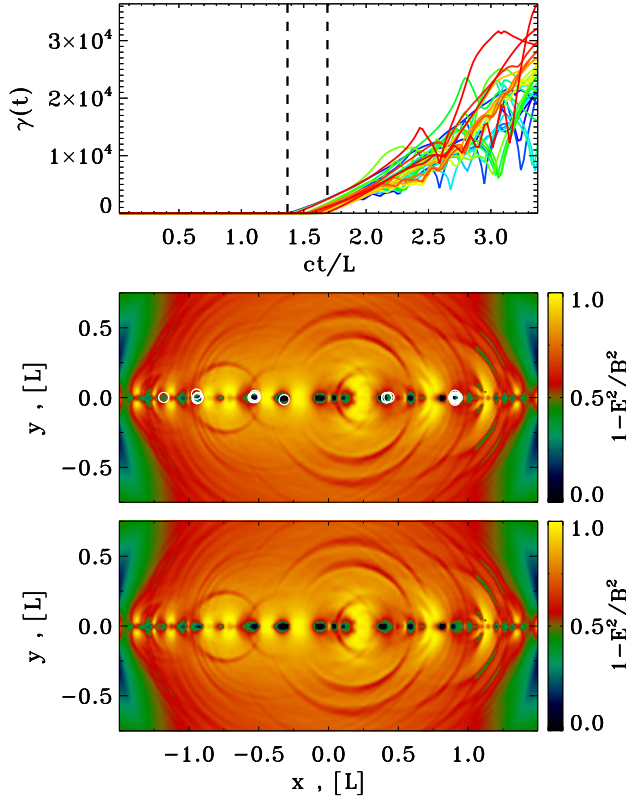
Fig. 9 Physics of particle injection into the acceleration process, from a PIC simulation of stressed X-point collapse with vanishing guide field and $\sigma = 4 \times 10^2$ (Lyutikov et al 2016b). Top panel: we select all the particles that exceed the threshold $\gamma_0 = 30$ within a given time interval (chosen to be $1.4 \leq ct_0/L \leq 1.7$, as indicated by the vertical dashed lines), and we plot the temporal evolution of the Lorentz factor of the 30 particles that at the final time reach the highest energies. The particle Lorentz factor increases as $\gamma \propto t^2 - t_0^2$, where t_0 marks the onset of acceleration (i.e., the time when γ first exceeds γ_0). Middle panel: for the same particles as in the top panel, we plot their locations at the onset of acceleration with open white circles, superimposed over the 2D plot of $1 - E^2/B^2$ (more precisely, of $\max[0, 1 - E^2/B^2]$). Comparison of the middle panel with the bottom panel shows that particle injection is localized in the vicinity of the X-points in the current sheet (i.e., the blue regions where $E > B$).

speed is quite small (red line in the middle panel of Fig. 11) and no significant energy exchange has occurred from the fields to the particles (compare the in-plane magnetic energy, shown by the dashed blue line in the top panel of Fig. 11, with the particle kinetic energy, indicated with the red line).

As a result of reconnection, an increasing number of field lines, that initially closed around one of the ropes, are now engulfing both magnetic islands. Their tension force causes the two ropes to approach and merge on a quick (dynamical) timescale, starting at $ct/r_j \sim 4.5$ and ending at $ct/r_j \sim 7.5$ (see that the distance of the rightmost island from the center rapidly decreases, as indicated by the black line in the middle panel of Fig. 11). The tension force drives the particles in the flux
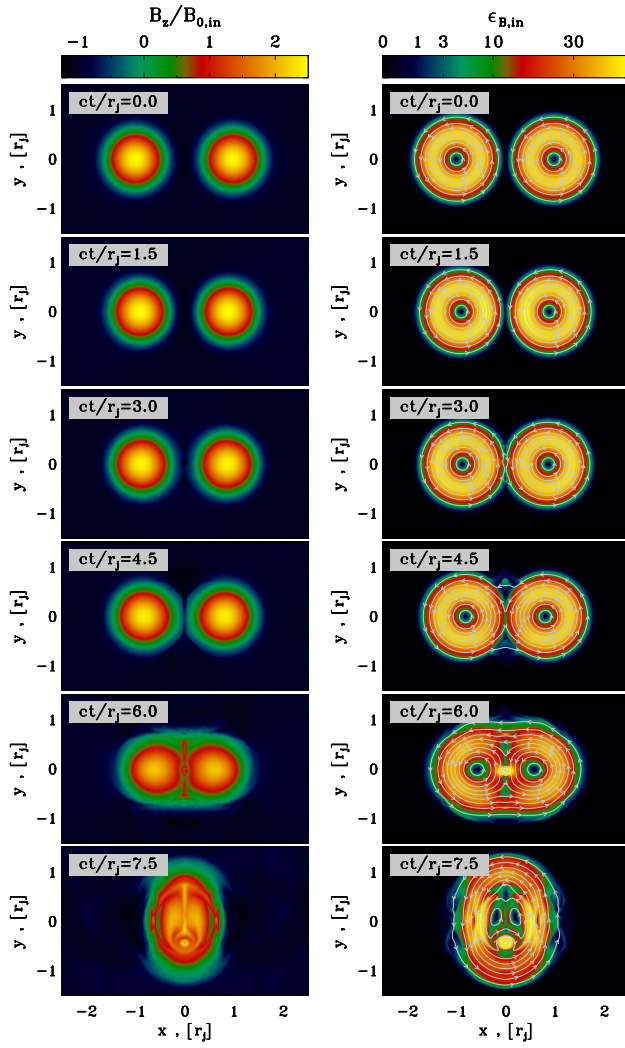
Fig. 10 Temporal evolution of 2D Lundquist ropes (time is measured in c/r_j and indicated in the grey box of each panel, increasing from top to bottom), from Lyutikov et al (2016b). The plot presents the 2D pattern of the out-of-plane field B_z (left column) and of the in-plane magnetic energy fraction $\epsilon_{B,in} = (B_x^2 + B_y^2)/8\pi n m c^2$ (right column; with superimposed magnetic field lines), from a PIC simulation with $kT/mc^2 = 10^{-4}$, $\sigma_{in} = 43$ and $r_j = 61\, r_{L,hot}$.

ropes toward the center, with a fast reconnection speed peaking at $v_{rec}/c \sim 0.3$ (red line in the middle panel of Fig. 11). The reconnection layer at $x = 0$ stretches up to a length of $\sim 2\, r_j$, and secondary plasmoids are formed. In the central current sheet, it is primarily the in-plane field that gets dissipated (compare the dashed and solid blue lines in the top panel of Fig. 11), driving an increase in the electric energy (green) and in the particle kinetic energy (red). In this phase of evolution, the fraction of initial energy released to the particles is small ($\epsilon_{kin}/\epsilon_{tot}(0) \sim 0.1$), but the particles advected into the central X-point experience a dramatic episode
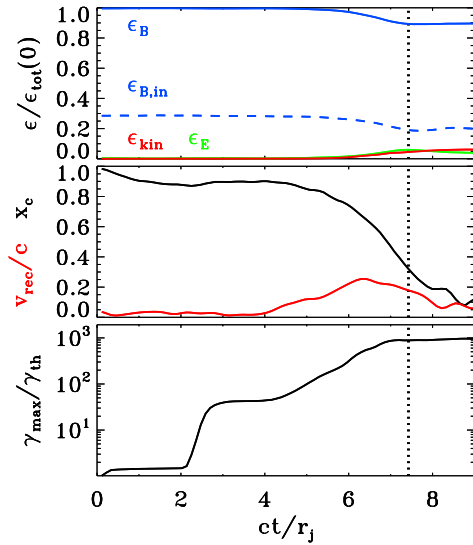
Fig. 11 Temporal evolution of various quantities, from a 2D PIC simulation of Lundquist ropes with $kT/mc^2 = 10^{-4}$, $\sigma_{in} = 43$ and $r_j = 61\,r_{L,hot}$ (the same as in Fig. 10), from Lyutikov et al (2016b). Top panel: fraction of energy in magnetic fields (solid blue), in-plane magnetic fields (dashed blue), electric fields (green) and particles (red; excluding the rest mass energy), in units of the total initial energy. Middle panel: reconnection rate v_{rec}/c (red), and location x_c of the core of the rightmost flux rope (black), in units of r_j. Bottom panel: evolution of the maximum Lorentz factor γ_{max}.

of acceleration. As shown in the bottom panel of Fig. 11, the cutoff Lorentz factor γ_{max} of the particle spectrum presents a dramatic evolution, increasing up to $\gamma_{max}/\gamma_{th} \sim 10^3$ within a couple of dynamical times. This phase of extremely fast particle acceleration on a dynamical timescale is analogous to the relaxation of unstable force-free structures discussed above.

7 Future Directions

7.1 Observation

Much has been learned in recent years from observations throughout the electromagnetic spectrum (radio through TeV γ-rays) and beyond (gravitational radiation, neutrinos and cosmic rays). Even more discoveries are anticipated from observations with new facilities that should come on line in the next ~ 5 years. Perhaps the most exciting opportunity is to make a (temporal) match of a short GRB with a LIGO event. Equally interesting would be a temporal association of an "cosmogenic" VHE neutrino with some other cosmic event. We may also learn about the details of jet production in AGN from Event Horizon Telescope observations of M87, as discussed above. Fast Radio Bursts are starting to reveal their secrets and they, too, may be shown to have some physical affinity with the other examples of release of energy, in particular magnetars. Comparisons of radio pulsar

observations with corresponding γ-ray observations and studies of radio scintillation are providing a much better understanding of neutron star magnetospheres which may help us calibrate our models of other magnetically dominant sources. Similar remarks apply to solar flares where there can be a rapid release of magnetic energy in a very short space of time.

There will also be new optical/near infrared survey telescopes devoted to transient astronomy including the Zwicky Transient Factory, LSST and Euclid, greatly increasing our ability to monitor familiar types of transient, as well as discover new classes of which we are now ignorant.

7.2 Simulation

With the advance in algorithms, simulation techniques and computational power, much more can be understood about plasma physics under extreme conditions using simulations. On one hand, fluid level simulations are now able to handle complex, realistic astrophysical situations, like the merging of neutron stars/black holes, tidal disruption events, colliding winds in binary systems, accretion disk and jet formation, etc. These provide more physical interpretation of the observed phenomena, also point to possible sites and mechanisms of dissipation and particle acceleration.

On the other hand, kinetic simulations are getting close to modeling multi-scale systems. For example, the role of reconnection and particle acceleration in accretion disk has been recently discussed in PIC simulations (e.g. Hoshino 2015; Riquelme et al 2012). PIC simulations are also used to study global pulsar magnetospheres (e.g., Chen and Beloborodov 2014; Belyaev 2015; Cerutti et al 2015; Philippov et al 2015), relativistic turbulence (Zhdankin et al 2017), etc. Improved hybrid methods are also bridging between the kinetic and macroscopic length scales (Kunz et al 2016). A major challenge is to increase the dynamic range of particle energy that can be covered in these simulations to approach that found in the sources discussed above. Furthermore, new physics is being added to traditional PIC simulations, including pair production (Chen and Beloborodov 2014), general relativistic effect (Philippov et al 2015), radiative feedback (Uzdensky 2016), and hadronic interactions.

7.3 Experiment

Another new development is the prospect of performing novel experiments at the many powerful light sources around the world that are already operational or are expected to become such over the next five years. There are various schemes being explored. For example, γ-rays can be created by Bethe-Heitler bremsstrahlung when a relativistic electron beam interacts with a foil target. Electron-positron pairs will also be produced. However if the γ-rays are above threshold they can also pair-produce on an oncoming, coherent X-ray beam from a powerful laser by the Breit-Wheeler process, just like in cosmic sources. Achieving this pair production will be a major experimental milestone but will have no significance for QED as the cross-section is not in doubt! However, it will open the door to explorations of nonlinear quantum electrodynamics where calculations are hard and deserve

validation. In addition and of even more interest for astrophysics are the many body processes where it is the collective properties of the pair plasma that are important. There are additional processes that can be investigated in the same spirit involving large magnetostatic fields.

These explorations, although partly inspired by the challenges of extreme astrophysical acceleration, will be prosecuted in the spirit of comparing experiments that can be performed and diagnosed with numerical simulations. It is an exciting prospect that new effects will be discovered and that some of these may have a role in understanding the processes we have discussed in this chapter.

References

Ackermann M, Anantua R, Asano K, et al (2016) Minute-timescale >100 MeV γ-Ray Variability during the Giant Outburst of Quasar 3C 279 Observed by Fermi-LAT in 2015 June. Astrophys. J. Lett. 824:L20, DOI 10.3847/2041-8205/824/2/L20, 1605.05324

Aharonian F, Akhperjanian AG, Bazer-Bachi AR, et al (2007) An Exceptional Very High Energy Gamma-Ray Flare of PKS 2155-304. Astrophys. J. Lett. 664:L71–L74, DOI 10.1086/520635, 0706.0797

Albert J, Aliu E, Anderhub H, et al (2007) Variable Very High Energy γ-Ray Emission from Markarian 501. Astrophys. J. 669:862–883, DOI 10.1086/521382, astro-ph/0702008

Aleksić J, Antonelli LA, Antoranz P, et al (2011) MAGIC Discovery of Very High Energy Emission from the FSRQ PKS 1222+21. Astrophys. J. Lett. 730:L8, DOI 10.1088/2041-8205/730/1/L8, 1101.4645

Arnol'd V (1965) Sur la topologie des bcoulements stationnaires des fluides parfaits. CRA d SciParis 261:17–20

Arons J (2003) Magnetars in the Metagalaxy: An Origin for Ultra-High-Energy Cosmic Rays in the Nearby Universe. Astrophys. J. 589:871–892, DOI 10.1086/374776, astro-ph/0208444

Arons J (2012) Pulsar Wind Nebulae as Cosmic Pevatrons: A Current Sheet's Tale. Space Sci. Rev. 173:341–367, DOI 10.1007/s11214-012-9885-1, 1208.5787

Begelman MC, Ergun RE, Rees MJ (2005) Cyclotron Maser Emission from Blazar Jets? Astrophys. J. 625:51–59, DOI 10.1086/429550, astro-ph/0502151

Begelman MC, Fabian AC, Rees MJ (2008) Implications of very rapid TeV variability in blazars. Mon. Not. R. astr. Soc. 384:L19–L23, DOI 10.1111/j.1745-3933.2007.00413.x, 0709.0540

Bellan PM (2000) Spheromaks: a practical application of magnetohydrodynamic dynamos and plasma self-organization. Imperial College Press, London

Beltrami E (1902) Opere matematiche. Milano

Belyaev MA (2015) Dissipation, energy transfer, and spin-down luminosity in 2.5D PIC simulations of the pulsar magnetosphere. Mon. Not. R. astr. Soc. 449:2759–2767, DOI 10.1093/mnras/stv468, 1412.2819

Biskamp D (2000) Magnetic reconnection in plasmas. Cambridge University Press, Cambridge

Blandford R, Simeon P, Yuan Y (2014) Cosmic Ray Origins: An Introduction. Nuclear Physics B Proceedings Supplements 256:9–22, DOI 10.1016/j.nuclphysbps.2014.10.002, URL http://adsabs.harvard.edu/abs/2014NuPhS.256....9B

Blandford R, East W, Nalewajko K, Yuan Y, Zrake J (2015) Active Galactic Nuclei: The TeV Challenge. arXiv:151107515 [astro-ph] URL http://arxiv.org/abs/1511.07515, arXiv:1511.07515

Blandford RD, Begelman MC (1999) On the fate of gas accreting at a low rate on to a black hole. Mon. Not. R. astr. Soc. 303:L1–L5, DOI 10.1046/j.1365-8711.1999.02358.x, astro-ph/9809083

Blandford RD, Königl A (1979) Relativistic jets as compact radio sources. Astrophys. J. 232:34–48, DOI 10.1086/157262

Blandford RD, Levinson A (1995) Pair cascades in extragalactic jets. 1: Gamma rays. Astrophys. J. 441:79–95, DOI 10.1086/175338

Boggs SE, Zoglauer A, Bellm E, et al (2007) The Giant Flare of 2004 December 27 from SGR 1806-20. Astrophys. J. 661:458–467, DOI 10.1086/516732, `astro-ph/0611318`

Brenner MP, Hilgenfeldt S, Lohse D (2002) Single-bubble sonoluminescence. Rev Mod Phys 74:425–484, DOI 10.1103/RevModPhys.74.425, URL `https://link.aps.org/doi/10.1103/RevModPhys.74.425`

Broderick AE, Narayan R, Kormendy J, et al (2015) The Event Horizon of M87. Astrophys. J. 805:179, DOI 10.1088/0004-637X/805/2/179, `1503.03873`

Buehler R, Blandford R (2014) The surprising Crab pulsar and its nebula: a review. Reports on Progress in Physics 77(6):066901, DOI 10.1088/0034-4885/77/6/066901, `1309.7046`

Burbidge GR (1956) On Synchrotron Radiation from Messier 87. Astrophys. J. 124:416, DOI 10.1086/146237

Cerutti B, Werner GR, Uzdensky DA, Begelman MC (2013) Simulations of Particle Acceleration beyond the Classical Synchrotron Burnoff Limit in Magnetic Reconnection: An Explanation of the Crab Flares. Astrophys. J. 770:147, DOI 10.1088/0004-637X/770/2/147, `1302.6247`

Cerutti B, Werner GR, Uzdensky DA, Begelman MC (2014) Three-dimensional Relativistic Pair Plasma Reconnection with Radiative Feedback in the Crab Nebula. Astrophys. J. 782:104, DOI 10.1088/0004-637X/782/2/104, `1311.2605`

Cerutti B, Philippov A, Parfrey K, Spitkovsky A (2015) Particle acceleration in axisymmetric pulsar current sheets. Mon. Not. R. astr. Soc. 448:606–619, DOI 10.1093/mnras/stv042, `1410.3757`

Chandrasekhar S, Kendall PC (1957) On Force-Free Magnetic Fields. Astrophys. J. 126:457, DOI 10.1086/146413

Chen AY, Beloborodov AM (2014) Electrodynamics of Axisymmetric Pulsar Magnetosphere with Electron-Positron Discharge: A Numerical Experiment. Astrophys. J. Lett. 795:L22, DOI 10.1088/2041-8205/795/1/L22, `1406.7834`

Childress S (1970) New Solutions of the Kinematic Dynamo Problem. Journal of Mathematical Physics 11:3063–3076, DOI 10.1063/1.1665095

Drake JF, Swisdak M, Che H, Shay MA (2006) Electron acceleration from contracting magnetic islands during reconnection. Nature 443:553–556, DOI 10.1038/nature05116

East WE, Zrake J, Yuan Y, Blandford RD (2015) Spontaneous Decay of Periodic Magnetostatic Equilibria. Physical Review Letters 115(9):095002, DOI 10.1103/PhysRevLett.115.095002, `1503.04793`

Evans WD, Klebesadel RW, Laros JG, et al (1980) Location of the gamma-ray transient event of 1979 March 5. Astrophys. J. Lett. 237:L7–L9, DOI 10.1086/183222

Fanaroff BL, Riley JM (1974) The morphology of extragalactic radio sources of high and low luminosity. Mon. Not. R. astr. Soc. 167:31P–36P, DOI 10.1093/mnras/167.1.31P

Fish VL, Johnson MD, Doeleman SS, et al (2016) Persistent Asymmetric Structure of Sagittarius A* on Event Horizon Scales. Astrophys. J. 820:90, DOI 10.3847/0004-637X/820/2/90, `1602.05527`

Furth HP, Killeen J, Rosenbluth MN (1963) Finite-Resistivity Instabilities of a Sheet Pinch. Physics of Fluids 6:459–484, DOI 10.1063/1.1706761

Giacconi R, Gursky H, Paolini FR, Rossi BB (1962) Evidence for x Rays From Sources Outside the Solar System. Physical Review Letters 9:439–443, DOI 10.1103/PhysRevLett.9.439

Gold T (1955) Concluding Remarks on Turbulence in the Interstellar Gas. In: Gas Dynamics of Cosmic Clouds, IAU Symposium, vol 2, p 238

Guo F, Li H, Daughton W, Liu YH (2014) Formation of Hard Power Laws in the Energetic Particle Spectra Resulting from Relativistic Magnetic Reconnection. Physical Review Letters 113(15):155005, DOI 10.1103/PhysRevLett.113.155005, `1405.4040`

Hess VF (1912) Observations of the penetrating radiation on seven balloon flights. Physik Zeitschr 13:1084–1091

Hester JJ (2008) The Crab Nebula: An Astrophysical Chimera. Annu. Rev. Astron. Astr. 46:127–155, DOI 10.1146/annurev.astro.45.051806.110608

Hester JJ, Scowen PA, Sankrit R, et al (1995) WFPC2 Studies of the Crab Nebula. I. HST and ROSAT Imaging of the Synchrotron Nebula. Astrophys. J. 448:240, DOI 10.1086/175956

Hewish A, Bell SJ, Pilkington JDH, Scott PF, Collins RA (1968) Observation of a Rapidly Pulsating Radio Source. Nature 217:709–713, DOI 10.1038/217709a0

Horton W, Tajima T (1988) Linear theory of driven reconnection. J. Geophys. Res. 93:2741–2748, DOI 10.1029/JA093iA04p02741

Hoshino M (2012) Stochastic Particle Acceleration in Multiple Magnetic Islands during Reconnection. Physical Review Letters 108(13):135003, DOI 10.1103/PhysRevLett.108.135003, `1201.0837`

Hoshino M (2015) Angular Momentum Transport and Particle Acceleration During Magnetorotational Instability in a Kinetic Accretion Disk. Physical Review Letters 114(6):061101, DOI 10.1103/PhysRevLett.114.061101, `1502.02452`

Hoshino M, Mukai T, Terasawa T, Shinohara I (2001) Suprathermal electron acceleration in magnetic reconnection. J. Geophys. Res. 106:25,979–25,998, DOI 10.1029/2001JA900052

Hurley K, Cline T, Mazets E, et al (1999) A giant periodic flare from the soft γ-ray repeater SGR1900+14. Nature 397:41–43, DOI 10.1038/16199, `astro-ph/9811443`

Hurley K, Boggs SE, Smith DM, et al (2005) An exceptionally bright flare from SGR 1806-20 and the origins of short-duration γ-ray bursts. Nature 434:1098–1103, DOI 10.1038/nature03519, `astro-ph/0502329`

Imshennik VS, Syrovatskiĭ SI (1967) Two-dimensional Flow of an Ideally Conducting Gas in the Vicinity of the Zero Line of a Magnetic Field. Soviet Journal of Experimental and Theoretical Physics 25:656

Kagan D, Sironi L, Cerutti B, Giannios D (2015) Relativistic Magnetic Reconnection in Pair Plasmas and Its Astrophysical Applications. Space Sci. Rev. 191:545–573, DOI 10.1007/s11214-014-0132-9, `1412.2451`

Kaspi VM, Beloborodov A (2017) Magnetars. Annu. Rev. Astron. Astr. , in press `arXiv:1703.00068`

Kennel CF, Coroniti FV (1984) Magnetohydrodynamic model of Crab nebula radiation. Astrophys. J. 283:710–730, DOI 10.1086/162357

Kirk JG, Lyubarsky Y, Petri J (2009) The Theory of Pulsar Winds and Nebulae. In: Becker W (ed) Astrophysics and Space Science Library, Astrophysics and Space Science Library, vol 357, p 421, `astro-ph/0703116`

Klebesadel RW, Strong IB, Olson RA (1973) Observations of Gamma-Ray Bursts of Cosmic Origin. Astrophys. J. Lett. 182:L85, DOI 10.1086/181225

Komissarov SS, Lyubarsky YE (2003) The origin of peculiar jet-torus structure in the Crab nebula. Mon. Not. R. astr. Soc. 344:L93–L96, DOI 10.1046/j.1365-8711.2003.07097.x, `astro-ph/0306162`

Komissarov SS, Lyubarsky YE (2004) Synchrotron nebulae created by anisotropic magnetized pulsar winds. Mon. Not. R. astr. Soc. 349:779–792, DOI 10.1111/j.1365-2966.2004.07597.x

Komissarov SS, Lyutikov M (2011) On the origin of variable gamma-ray emission from the Crab nebula. Mon. Not. R. astr. Soc. 414:2017–2028, DOI 10.1111/j.1365-2966.2011.18516.x, `1011.1800`

Kouveliotou C, Wijers RAMJ, Woosley S (2012) Gamma-ray Bursts. Cambridge University Press, Cambridge, UK, URL `http://adsabs.harvard.edu/abs/2012grb..book.....K`

Kunz MW, Stone JM, Quataert E (2016) Magnetorotational Turbulence and Dynamo in a Collisionless Plasma. Physical Review Letters 117(23):235101, DOI 10.1103/PhysRevLett.117.235101, `1608.07911`

Levinson A, Blandford R (1995) Raman scattering in high-radio-brightness astrophysical systems: application to active galactic nuclei. Mon. Not. R. astr. Soc. 274:717–729, DOI 10.1093/mnras/274.3.717

Lohse D, Schmitz B, Versluis M (2001) Snapping shrimp make flashing bubbles. Nature 413(6855):477–478, DOI 10.1038/35097152, URL `http://www.nature.com/nature/journal/v413/n6855/abs/413477a0.html`

Lorimer DR, Bailes M, McLaughlin MA, Narkevic DJ, Crawford F (2007) A Bright Millisecond Radio Burst of Extragalactic Origin. Science 318:777, DOI 10.1126/science.1147532, `0709.4301`

Lyutikov M, Balsara D, Matthews C (2012) Crab GeV flares from the corrugated termination shock. Mon. Not. R. astr. Soc. 422:3118–3129, DOI 10.1111/j.1365-2966.2012.20831.x, `1109.1204`

Lyutikov M, Komissarov SS, Porth O (2016a) The inner knot of the Crab nebula. Mon. Not. R. astr. Soc. 456:286–299, DOI 10.1093/mnras/stv2570, `1506.07282`

Lyutikov M, Sironi L, Komissarov S, Porth O (2016b) Particle acceleration in explosive relativistic reconnection events and Crab Nebula gamma-ray flares. ArXiv e-prints 1603.05731

Madejski G, Sikora M (2016) Gamma-Ray Observations of Active Galactic Nuclei. Annu. Rev. Astron. Astr. 54:725–760, DOI 10.1146/annurev-astro-081913-040044

Marscher AP, Jorstad SG, D'Arcangelo FD, et al (2008) The inner jet of an active galactic nucleus as revealed by a radio-to-γ-ray outburst. Nature 452:966–969, DOI 10.1038/nature06895

Max-Moerbeck W, Hovatta T, Richards JL, et al (2014) Time correlation between the radio and gamma-ray activity in blazars and the production site of the gamma-ray emission. Mon. Not. R. astr. Soc. 445:428–436, DOI 10.1093/mnras/stu1749, 1408.6264

Meier DL (2012) Black Hole Astrophysics: The Engine Paradigm. Springer, Verlag Berlin Heidelberg, URL http://adsabs.harvard.edu/abs/2012bhae.book.....M

Mereghetti S, Götz D, Mirabel IF, Hurley K (2005) INTEGRAL discovery of persistent hard X-ray emission from the Soft Gamma-ray Repeater SGR 1806-20. Astron. Astrophys. 433:L9–L12, DOI 10.1051/0004-6361:200500088, astro-ph/0411695

Mirabel IF, Rodríguez LF (1999) Sources of Relativistic Jets in the Galaxy. Annu. Rev. Astron. Astr. 37:409–443, DOI 10.1146/annurev.astro.37.1.409, astro-ph/9902062

Moffatt HK (1978) Magnetic field generation in electrically conducting fluids. Cambridge University Press, Cambridge, England, URL http://adsabs.harvard.edu/abs/1978mfge.book.....M

Moffatt HK (1986) Magnetostatic equilibria and analogous Euler flows of arbitrarily complex topology. II - Stability considerations. Journal of Fluid Mechanics 166:359–378, DOI 10.1017/S0022112086000198

Nalewajko K, Zrake J, Yuan Y, East WE, Blandford RD (2016) Kinetic Simulations of the Lowest-order Unstable Mode of Relativistic Magnetostatic Equilibria. Astrophys. J. 826:115, DOI 10.3847/0004-637X/826/2/115, 1603.04850

Parker EN (1963) The Solar-Flare Phenomenon and the Theory of Reconnection and Annihilation of Magnetic Fields. Astrophys. J. Suppl. S. 8:177, DOI 10.1086/190087

Petschek HE (1964) Magnetic Field Annihilation. NASA Special Publication 50:425

Philippov AA, Cerutti B, Tchekhovskoy A, Spitkovsky A (2015) Ab Initio Pulsar Magnetosphere: The Role of General Relativity. Astrophys. J. Lett. 815:L19, DOI 10.1088/2041-8205/815/2/L19, 1510.01734

Priest E, Forbes T (2000) Magnetic Reconnection: MHD Theory and Applications. Cambridge University Press, Cambridge, URL http://ebooks.cambridge.org/ebook.jsf?bid=CBO9780511525087

Reber G, Greenstein JL (1947) Radio-frequency investigations of astronomical interest. The Observatory 67:15–26

Rees MJ, Gunn JE (1974) The origin of the magnetic field and relativistic particles in the Crab Nebula. Mon. Not. R. astr. Soc. 167:1–12

Reid MJ, Biretta JA, Junor W, Muxlow TWB, Spencer RE (1989) Subluminal motion and limb brightening in the nuclear jet of M87. Astrophys. J. 336:112–120, DOI 10.1086/166998

Riquelme MA, Quataert E, Sharma P, Spitkovsky A (2012) Local Two-dimensional Particle-in-cell Simulations of the Collisionless Magnetorotational Instability. Astrophys. J. 755:50, DOI 10.1088/0004-637X/755/1/50, 1201.6407

Rosenbluth MN, Bussac MN (1979) MHD stability of Spheromak. Nuclear Fusion 19:489–498

Rudy A, Horns D, DeLuca A, et al (2015) Characterization of the Inner Knot of the Crab: The Site of the Gamma-Ray Flares? Astrophys. J. 811:24, DOI 10.1088/0004-637X/811/1/24, 1504.04613

Schmidt M (1963) 3C 273 : A Star-Like Object with Large Red-Shift. Nature 197:1040, DOI 10.1038/1971040a0

Sironi L, Spitkovsky A (2009) Particle Acceleration in Relativistic Magnetized Collisionless Pair Shocks: Dependence of Shock Acceleration on Magnetic Obliquity. Astrophys. J. 698:1523–1549, DOI 10.1088/0004-637X/698/2/1523, 0901.2578

Sironi L, Spitkovsky A (2011a) Acceleration of Particles at the Termination Shock of a Relativistic Striped Wind. Astrophys. J. 741:39, DOI 10.1088/0004-637X/741/1/39, 1107.0977

Sironi L, Spitkovsky A (2011b) Particle Acceleration in Relativistic Magnetized Collisionless Electron-Ion Shocks. Astrophys. J. 726:75, DOI 10.1088/0004-637X/726/2/75, 1009.0024

Sironi L, Spitkovsky A (2014) Relativistic Reconnection: An Efficient Source of Non-thermal Particles. Astrophys. J. Lett. 783:L21, DOI 10.1088/2041-8205/783/1/L21, 1401.5471

Speiser TW (1965) Particle Trajectories in Model Current Sheets, 1, Analytical Solutions. J. Geophys. Res. 70:4219–4226, DOI 10.1029/JZ070i017p04219

Spitkovsky A (2008) Particle Acceleration in Relativistic Collisionless Shocks: Fermi Process at Last? Astrophys. J. Lett. 682:L5, DOI 10.1086/590248, 0802.3216

Syrovatskii SI (1966) Dynamic Dissipation of a Magnetic Field and Particle Acceleration. Soviet Astronomy10:270

Tait PG (1907) Properties of Matter. A. and C. Black

Taylor JB (1974) Relaxation of Toroidal Plasma and Generation of Reverse Magnetic Fields. Physical Review Letters 33(19):1139–1141, DOI 10.1103/PhysRevLett.33.1139, URL http://link.aps.org/doi/10.1103/PhysRevLett.33.1139

Taylor JB (1986) Relaxation and magnetic reconnection in plasmas. Reviews of Modern Physics 58(3):741–763, DOI 10.1103/RevModPhys.58.741, URL http://link.aps.org/doi/10.1103/RevModPhys.58.741

Thompson C, Duncan RC (1995) The soft gamma repeaters as very strongly magnetized neutron stars - I. Radiative mechanism for outbursts. Mon. Not. R. astr. Soc. 275:255–300, DOI 10.1093/mnras/275.2.255

Thompson C, Duncan RC (1996) The Soft Gamma Repeaters as Very Strongly Magnetized Neutron Stars. II. Quiescent Neutrino, X-Ray, and Alfven Wave Emission. Astrophys. J. 473:322, DOI 10.1086/178147

Uzdensky DA (2016) Radiative Magnetic Reconnection in Astrophysics. Magnetic Reconnection: Concepts and Applications 427:473, DOI 10.1007/978-3-319-26432-5\textunderscore12, 1510.05397

Uzdensky DA, Cerutti B, Begelman MC (2011) Reconnection-powered Linear Accelerator and Gamma-Ray Flares in the Crab Nebula. Astrophys. J. Lett. 737:L40, DOI 10.1088/2041-8205/737/2/L40, 1105.0942

Wang X, Bhattacharjee A, Ma ZW (2000) Collisionless reconnection: Effects of Hall current and electron pressure gradient. J. Geophys. Res. 105:27,633–27,648, DOI 10.1029/1999JA000357

Weisskopf MC, Hester JJ, Tennant AF, et al (2000) Discovery of Spatial and Spectral Structure in the X-Ray Emission from the Crab Nebula. Astrophys. J. Lett. 536:L81–L84, DOI 10.1086/312733, astro-ph/0003216

Werner GR, Uzdensky DA, Cerutti B, Nalewajko K, Begelman MC (2016) The Extent of Power-law Energy Spectra in Collisionless Relativistic Magnetic Reconnection in Pair Plasmas. Astrophys. J. Lett. 816:L8, DOI 10.3847/2041-8205/816/1/L8, 1409.8262

Wilson-Hodge CA, Cherry ML, Case GL, et al (2011) When a Standard Candle Flickers. Astrophys. J. Lett. 727:L40, DOI 10.1088/2041-8205/727/2/L40, 1010.2679

Yuan F, Narayan R (2014) Hot Accretion Flows Around Black Holes. Annu. Rev. Astron. Astr. 52:529–588, DOI 10.1146/annurev-astro-082812-141003, 1401.0586

Yuan Y, Blandford RD (2015) On the implications of recent observations of the inner knot in the Crab nebula. Mon. Not. R. astr. Soc. 454:2754–2769, DOI 10.1093/mnras/stv2093, 1506.08121

Yuan Y, Nalewajko K, Zrake J, East WE, Blandford RD (2016) Kinetic Study of Radiation-reaction-limited Particle Acceleration During the Relaxation of Unstable Force-free Equilibria. Astrophys. J. 828:92, DOI 10.3847/0004-637X/828/2/92, 1604.03179

Zenitani S, Hoshino M (2001) The Generation of Nonthermal Particles in the Relativistic Magnetic Reconnection of Pair Plasmas. Astrophys. J. Lett. 562:L63–L66, DOI 10.1086/337972, 1402.7139

Zhdankin V, Werner GR, Uzdensky DA, Begelman MC (2017) Kinetic Turbulence in Relativistic Plasma: From Thermal Bath to Nonthermal Continuum. Physical Review Letters 118(5):055103, DOI 10.1103/PhysRevLett.118.055103, 1609.04851

Zrake J (2016) Crab Flares due to Turbulent Dissipation of the Pulsar Striped Wind. Astrophys. J. 823:39, DOI 10.3847/0004-637X/823/1/39, 1512.05426